# 1.20 Deep Earth Structure - Subduction Zone Structure in the Mantle Transition Zone

**Y Fukao and M Obayashi**, Japan Agency for Marine-Earth Science and Technology, Kanagawa, Japan

## 1.20.1 Introduction

During subduction, lithospheric plates are removed from Earth's surface by descent into the mantle from deep-sea trenches. The subducted part of the plate is called the slab. The slab is colder, and hence heavier, than the surrounding mantle, so the resultant negative buoyancy force is a major factor in driving plate motions. Subduction zones are deeper and less mobile than seafloor spreading centers, where oceanic plates are born. Slab descent in subduction zones along the Circum-Pacific represents a deep sheet-like downwelling of mantle convection, whereas magma ascent in spreading centers along midoceanic ridges is a shallow phenomenon, not corresponding directly to large-scale mantle upwelling. The seismic structure of the seafloor spreading centers has been discussed extensively by Dunn and Forsyth (2007).

A subducting slab is a downward continuation of the surface oceanic plate, marked seismologically by high P-wave and S-wave velocities and low P-wave and S-wave attenuations and geodynamically by low temperature, high density, and negative buoyancy relative to the surrounding mantle. The most reliable indicator of the subducting slab is the positive anomaly of seismic velocity. Figure 1 shows the depth profiles of the areal proportion of more than $x$% higher-than-normal velocities for several global P-wave and S-wave tomographic models, where $x = 0.5, 0.6, \ldots, 1.5$. The P-wave and S-wave models HMSL were obtained by measuring the travel times of long-period body wave phases by cross-correlation techniques. The S-wave model S362ANI was obtained by combining a large data set of surface-wave phase-velocity anomalies, long-period waveforms, and the body-wave travel times; S40RTS by measuring travel times of body waves, phase velocities of surface waves and splitting functions of normal modes from broadband waveform data; and TX2011 by measuring arrival times of multibounce shear waves, core-reflected shear waves, and SKS and SKKS waves (see Figure 4 of Dziewonski and Romanowicz (2007) for the nomenclature). The P-wave model MIT-P08 is based on reported and self-picked arrival times and waveform-based differential travel times for which the finite frequency effect (Kárason and van der Hilst, 2001) is taken into account; GAP_P4, on applying finite frequency kernels (Dahlen et al., 2000; Mercerat and Nolet, 2013) to all the datasets of reported and self-picked travel times and waveform-based differential travel times, including those from ocean-bottom seismometers; and LLNL-G3Dv3, on applying a global multiple event locator to reprocess the reported arrival times. See Thurber and Ritsema (2007) for the review of seismic tomography.

In Figure 1, all the model profiles exhibit extrema in the three depth ranges, the uppermost mantle, the transition zone, and the lowermost mantle, which are diagnostic of lithospheric plates on the surface, stagnant slabs in the transition zone (Fukao et al., 1992; van der Hilst et al., 1991), and slab graveyards at the bottom of the mantle (Richards and Engebretson, 1992), respectively. Indeed, the most outstanding feature of the transition zone in any of the recent tomographic models (see Figure 8 of Thurber and Ritsema (2007); see also Figure 2) is the extensive horizontal spread of fast anomalies beneath subduction zones, which has been interpreted as a signature of stagnant slabs.

We also note in Figure 1 that several models, for example, TX2011 and LLNL-G3Dv3, show a secondary peak in the uppermost lower mantle, just below the 660-km discontinuity. Although other models do not exhibit such a clear peak, they still show a richness of high-velocity anomaly signals in the uppermost lower mantle. This richness is an indication of
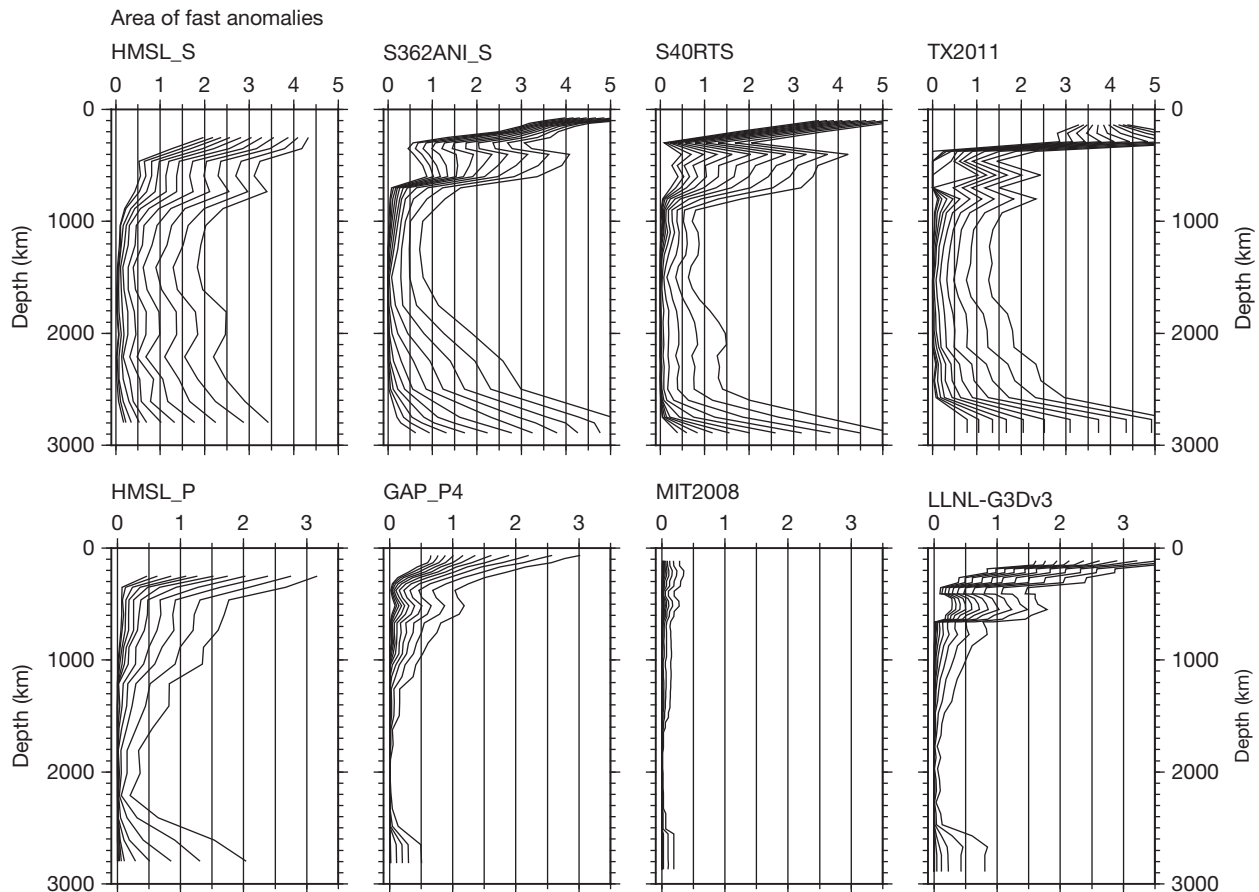
Area of fast anomalies



**Figure 1**   Depth profiles of the areal proportion of high-velocity anomalies in global tomographic models. The area at each depth is normalized so that its maximum is $4\pi$. The 16 profiles from right to left in each diagram represent the areal proportions of velocity anomalies 0.5%, 0.6%,..., 1.5% higher than normal. The S-wave velocity models in the upper column are HMSL (Houser et al., 2008a), S362ANI (Kustowski et al., 2008), S40RTS (Ritsema et al., 2011), and TX2011 (Grand, 2002). The P-wave velocity models in the lower column are HMSL (Houser et al., 2008a), GAP_P4 (Obayashi et al., 2013), MIT-P08 (Li et al., 2008), and LLNL-G3Dv3 (Simmons et al., 2012). Note a difference in scale between the S-wave and P-wave velocity models.

the slabs that penetrate the 660-km discontinuity and extend subhorizontally in the uppermost lower mantle. The mantle transition zone and the uppermost lower mantle are reviewed here as two distinct reservoirs, one for downgoing slabs above the 660-km discontinuity and the other for penetrating slabs below the discontinuity. Both reservoirs are not complete in the sense that slabs eventually descend well into the deep lower mantle (Grand et al., 1997; van der Hilst et al., 1997). We hope this chapter will be useful for discussing how significant the transition zone and the uppermost lower mantle are in the whole system of mantle convection. Wen and Anderson (1995, 1997) emphasized the unique role of the uppermost lower mantle in the system of mantle convection involving surface plate motions. Another intriguing feature to be noted in Figure 1, although not discussed in this chapter, is the depth of the least horizontal spread of high-velocity anomalies, which is systematically different between the P-wave and S-wave velocity perturbations, approximately 1500 km for all the four S-wave velocity models but approximately 2000 km for all the four P-wave velocity models.

## 1.20.2   Global View of Subduction Zone Structure in the Transition Zone

### 1.20.2.1   Seismic Velocity Anomalies

Masters et al. (1982) were the first to show that the structural heterogeneity in the transition zone is, to the first approximation, dominated by a degree-2 pattern with high-velocity anomalies beneath the Circum-Pacific subduction zones (see Figure 9 of Dziewonski and Romanowicz, 2007). **Figure 2** shows the velocity anomaly patterns at depths of ~500 km in the mantle transition zone for the eight models corresponding to those in **Figure 1** (see also Figure 3 of Panning and Romanowicz, 2006 for S-wave velocity anomalies and supplementary Figure 29(a) of Meer et al., 2009 for P-wave velocity anomalies). The most pronounced feature at these depths, both in the S-wave and in the P-wave velocity models, is the high-velocity signals in subduction zones, the strongest in the western Pacific (the northwestern Pacific in particular) and the next strongest in South America (southern South America in particular). The Pacific plate, the largest oceanic
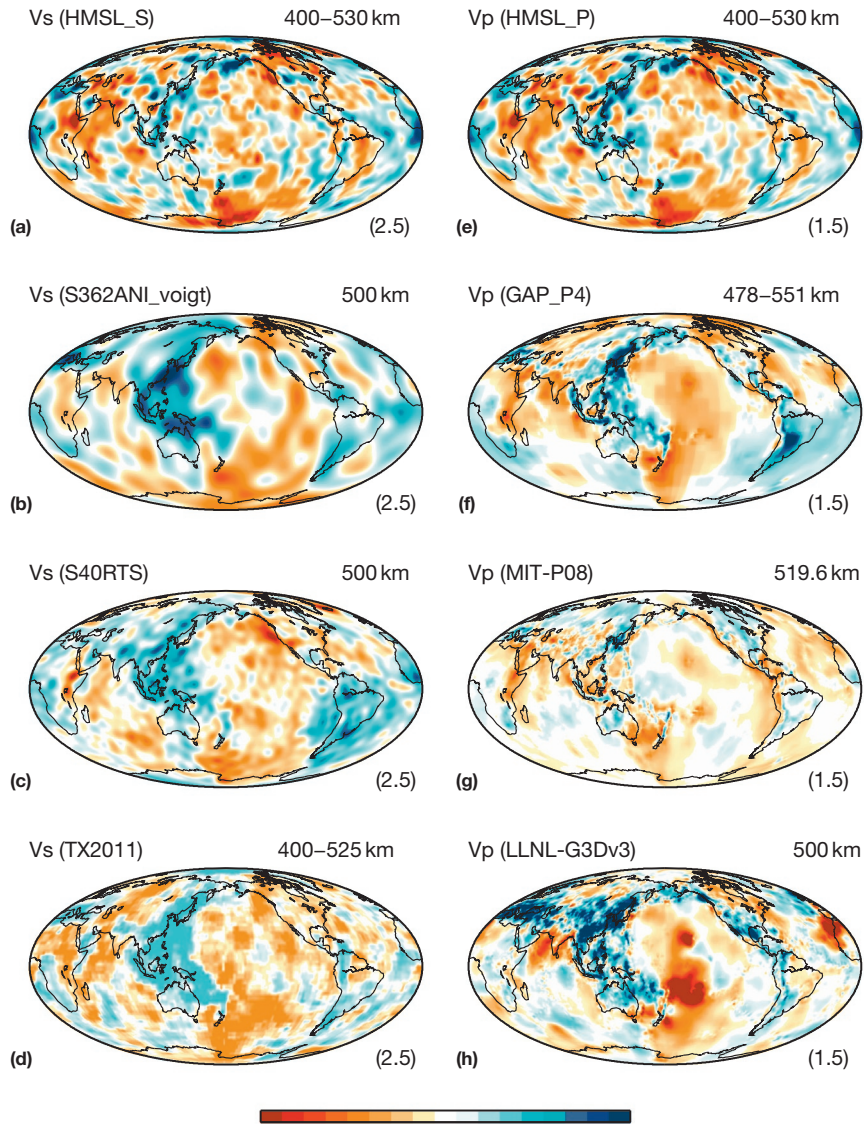
**Figure 2** Depth slices in the transition zone for the four S-wave and four P-wave velocity models corresponding to those in **Figure 1**. The velocities are perturbations from the average value at the corresponding depth. The scale is ±2.5% for the S-wave velocity models and ±1.5% for the P-wave velocity models.

plate, has continued to subduct beneath the western Pacific since the late Cretaceous Period, although its spreading direction changed greatly in the early Eocene Epoch (Lithgow-Bertelloni and Richard, 1998). The Indo-Australian plate, the second largest oceanic plate, has also continued to subduct beneath the western Pacific since the fusion of the Indian plate and Australian plate in the early Eocene (Lithgow-Bertelloni and Richard, 1998). The Nazca plate and the preceding Farallon plate have continued to rapidly subduct beneath South America since the early Eocene, without intermission by, for example, ridge subduction (Lithgow-Bertelloni and Richard, 1998). Clearly, the high-velocity anomalies beneath the western Pacific and South America reflect a long history of subductions of oceanic plates. Besides the Circum-Pacific subduction zones, the Mediterranean subduction zone is marked by the anomalously fast transition zone in all eight models. This high-velocity signature reflects the long history of

subduction of the Mediterranean lithosphere against the Eurasian plate since the late Cretaceous Period, including slow subduction in the first 20–30 My (Faccenna et al., 2001).

### 1.20.2.2 Boundary Topography

The mantle discontinuities at 410- and 660-km depths define the top and bottom of the mantle transition zone, across each of which P-wave and S-wave velocities and density increase sharply. These discontinuities are understood as the phase transition boundaries of major mantle minerals (see Stixrude and Jeanloz, 2007) that can be topographically distorted by a cold subducting slab. This subject has been reviewed by Kind and Li (2007). More recent studies include Schmerr and Thomas (2011) for Kurile, Schmerr and Garnero (2007) for South America, and Heit et al. (2010) and Gu et al. (2012) for the northwestern Pacific. Kind and Li (2007) summarized, for example, their review of the

Japan–Izu–Bonin subduction zones as follows. "The overwhelming majority of observations seem to indicate that the 660 is depressed at the Japanese subduction zone. The amount of the depression is ∼50 km. The 410 remains uncertain, but there is probably no clear elevation." Kind and Li (2007) further added, "Izu-Bonin seems, beside Japan, to be a good example of a depressed 660 at a slab. The uplift of the 410 seems less clear." The depression on the order of ∼50 km is likely to be the direct response of the 660-km discontinuity to the incoming slab from above. If the incoming slab bends to horizontal upon hitting the discontinuity to extend horizontally through the transition zone, we would expect a horizontal spread of the discontinuity depression, although the amount of depression may be smaller in the horizontally spreading part than in the directly downgoing part of the slab (e.g., Fukao et al., 2009).

The large lateral extent of the 660-km discontinuity depression was first observed by Shearer and Masters (1992) and Shearer (1993). **Figure 3** shows the three recent global topography maps for the 660-km discontinuity (see also Figure 6 of Kind and Li, 2007). The model of Houser et al. (2008b) (**Figure 3(a)**) is based on SS–SdS differential travel time measurements corrected for lateral heterogeneities of crustal thickness and upper mantle shear velocity, where SdS is a precursory reflection at depth d to the SS reflection at the surface. The model of Kustowski et al. (2008) (**Figure 3(b)**) is a part of the whole-mantle shear velocity model S362ANI (**Figure 2**) and was derived from the dataset that included SS-SdS differential times. The model of Meier et al. (2009) is not based on such depth phases as SdS, but relies on the sensitivities of overtone modes of Love waves and Rayleigh waves to the mantle discontinuity topography (**Figure 3(c)**). In these three models, the Circum-Pacific subduction zones are commonly characterized by long-wavelength depression of the 660-km discontinuity in qualitative agreement with the high-velocity anomaly pattern in the transition zone (**Figure 2**). Although the long-wavelength features are generally consistent among the three models, significant discrepancies are present as well, demonstrating the level of our understanding of the topography map of the 660-km discontinuity. Our understanding of the 410-km topography map is even less.

The reason for the less clear topographic feature of the 410-km discontinuity than the 660-km discontinuity may in part be the kinematically retarded olivine–wadsleyite transition across this discontinuity, which is expected to cause a narrow, wedge-like deepening of the phase boundary inside the cold slab (Kirby et al., 1996; Sung and Burns, 1976). A limited number of observational studies supporting the possible deepening of the phase boundary include travel time analyses by Iidaka and Suetsugu (1992) and Jiang et al. (2008) and a receiver function analysis by Kawakatsu and Yoshioka (2011) for the Honshu slab, a P-wave coda analysis by Kaneshima et al. (2007) for the Mariana slab, and a travel time analysis by Koper et al. (1998) for the Tonga slab. We are not yet at a stage where we can answer clearly whether the 410-km boundary inside the slab is elevated as expected for the phase transition at equilibrium or depressed as expected for the phase transition in a metastable state of olivine. The situation is quite different for the 660-km discontinuity, across which the phase transition from ringwoodite to ferromagnesian perovskite plus oxide should occur. In this case, the cold slab depresses the phase boundary at equilibrium, which may be further deepened by the retarded phase transition of ringwoodite in the cold environment (Fukao and Obayashi, 2013).
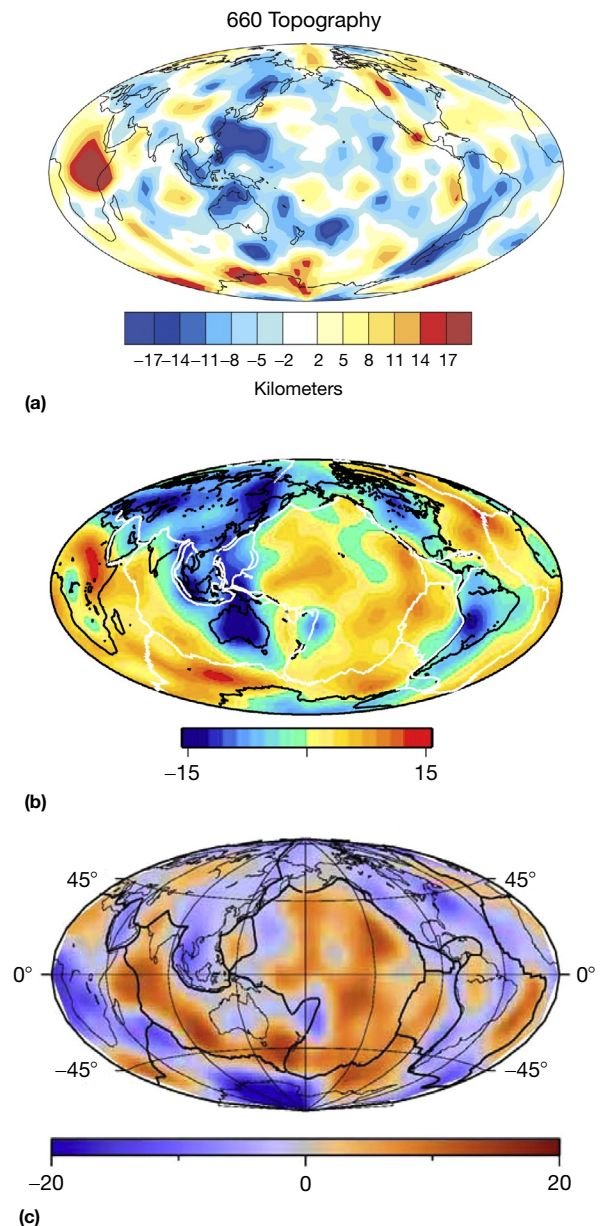


**Figure 3** Deviations from the average 660-km discontinuity depth for models (a) Houser C, Masters G, Flanagan M and Shearer P (2008b) Determination and analysis of long-wavelength transition zone structure using SS precursors. *Geophysical Journal International* 174: 178–194, (b) Kustowski B, Ekström G and Dziewonski AM (2008) Anisotropic shear–wave velocity structure of the Earth's mantle: A global model. *Journal of Geophysical Research* 113 (http://dx.doi.org/10.1029/2007JB005169), and (c) Meier U, Trampert J and Curtis A (2009) Global variations of temperature and water content in the mantle transition zone from higher mode surface waves. *Earth and Planetary Science Letters* 282: 91–101. Negative values (blue) indicate that the discontinuity is deeper than average and, likewise, positive values (red) indicate that it is shallower than average.

### 1.20.2.3 Seismic Attenuations

The horizontal spread of high-velocity anomalies also implies the dominance of high-Q anomalies in the transition zone beneath the subduction zone. Seismic $Q^{-1}$ is a measure of the degree of attenuation of a seismic wave. The progress

in attenuation studies has been slow because such studies typically rely on the amplitude measurement, which is affected by many factors, including determination of source mechanism, evaluation of focusing, defocusing, and scattering by structural heterogeneity, and correction for instrumental response. Such factors complicate interpretation of the measured amplitude in terms of attenuation. The current status of seismic attenuation studies of the structure of Earth is reviewed by Romanowicz and Mitchell (2007). Relatively recent global attenuation models include SW02 of Selby and Woodhouse (2002), QRLW8 of Gung and Romanowicz (2004), and QRFSI12 of Dalton et al. (2008). These models in the transition zone commonly show lower-than-normal attenuations beneath the western Pacific to eastern Asia, although the detail is quite different among the models. A counterpart of this subduction zone signal in the transition zone is the antipodal pair of high attenuation in the Pacific and in Africa, which was first demonstrated by Romanowicz (1990) from a Rayleigh wave analysis.

### 1.20.2.4    Seismic Anisotropy

The horizontal spread of high-velocity anomalies implies the dominance of horizontal shear flow in subduction zones, which might be detected by measuring radial seismic anisotropy in the transition zone beneath subduction zones (see Montagner, 2007). Unfortunately, resolving subduction zone characteristics of radial anisotropy from global mapping of radial anisotropy at depths near the bottom of the upper mantle remains a challenge (Ferreira et al., 2010; Kustowski et al., 2008; Lekić and Romanowicz, 2011; Panning and Romanowicz, 2006). Even the spherically averaged component of radial anisotropy is of marginal significance in this depth range, as may be understood by comparing several radial profiles of spherically averaged radial anisotropy presented in Figure 8 of Visser et al. (2008) and Figure 11 of Panning et al. (2010). Kawazoe et al. (2013) made a high pressure/temperature deformation experiment of wadsleyte, a major constituent mineral in the transition zone, to show that if the transition zone is dominated by horizontal shear flow, one would expect a spherically averaged radial anisotropy such that $V_{SH} < V_{SV}$ (horizontally polarized S waves are slower than vertically polarized S waves).

### 1.20.3    Slab Signatures Above and Below the 660-km Discontinuity

In this section, the cross-sectional views of subducted slabs above and below the 660-km discontinuity, that is, in the transition zone and in the uppermost lower mantle, are reviewed. The tomographic cross-sections along 11 profiles across Kurile (KR), Japan (JP), Bonin (BN), Mariana (MR), Java (JV), Tonga (TN), Kermadec (KM), northern and southern South America (nSA and sSA), and northern and middle Central America (nCA and mCA) for two P-wave velocity models, GAP_P4 of Obayashi et al. (2013) and LLNL-G3Dv3 of Simmons et al. (2012), and for two S-wave velocity models, S362ANI of Kustowski et al. (2008) and TX2011 of Grand (2002) are examined. Figure 4 shows the locations of these 11 profiles, which are chosen from Fukao and Obayashi (2013), who presented a number of equally spaced tomographic slices for each arc of the Circum-Pacific subduction zones. The P-wave images are scaled to $\pm1.5\%$ and the S-wave images to $\pm2.5\%$.

### 1.20.3.1    Slab Signature in the Transition Zone

Figure 5(a)–5(c) shows the tomographic cross-sections across Japan, Bonin, and southern South America, respectively, for the two P-wave velocity models and for the two S-wave velocity models. In these figures, the 410- and 660-km depth lines define the top and bottom of the transition zone. The 1000-km depth line is added as a measure of the bottom of the uppermost lower mantle, which is not a physically distinct boundary. The resolution of a subduction zone image is different between P-wave and S-wave velocity models. In general, first arrival time-based P-wave velocity models can resolve finer structures of subduction zones. On the other hand, a more uniform resolution is anticipated by broadband waveform-
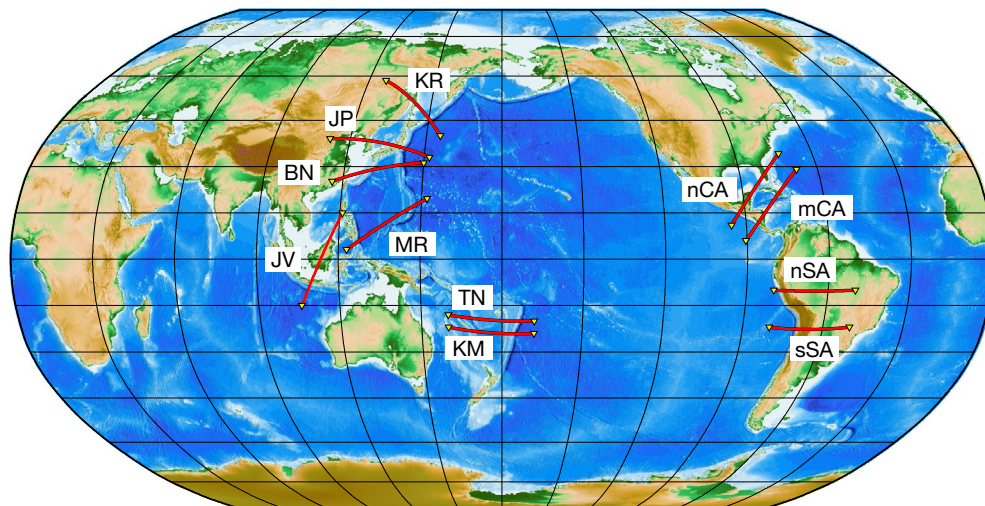


**Figure 4**    Location of the 11 profiles across typical subduction zones in the Circum-Pacific belt. The vertical cross-sections along these profiles are shown in **Figures 5** and **7–10**.

Japan

GAP_P4

LLNL-G3Dv3

S362ANI

TX2011

**(a)**

Bonin

GAP_P4

LLNL-G3Dv3

S362ANI

TX2011

**(b)**

Southern South America

GAP_P4

LLNL-G3Dv3

S362ANI

TX2011

**(c)**
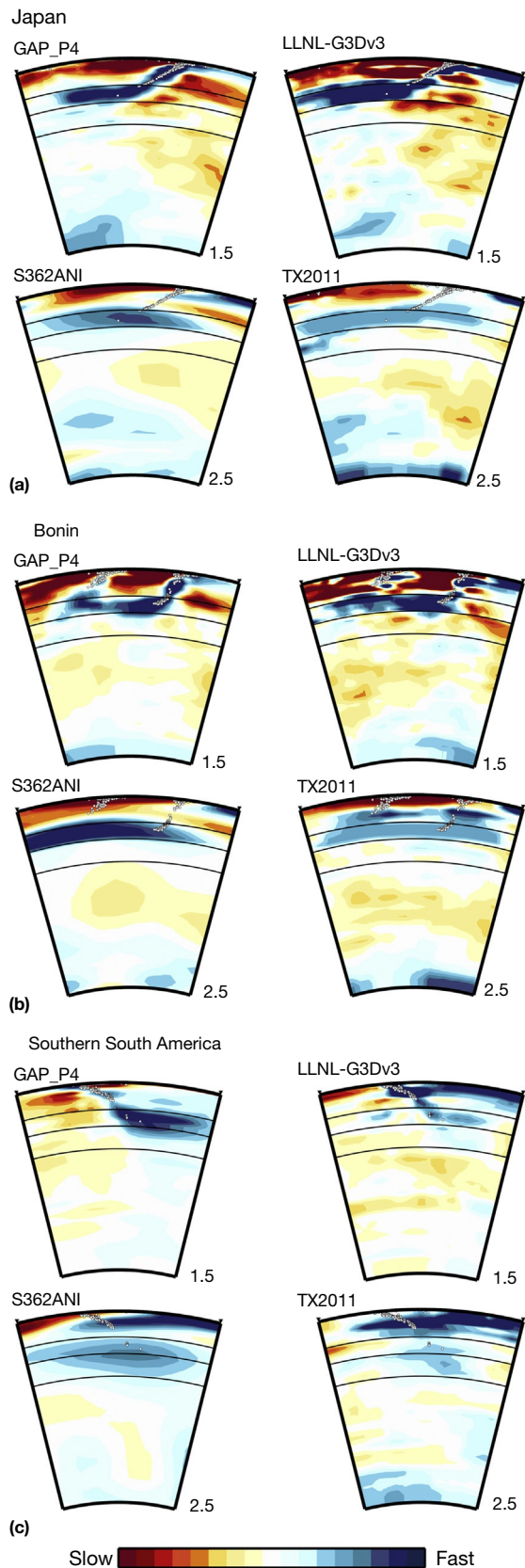
Slow ▓▓▓▓▓▓▓▓▓▓▓▓▓ Fast

**Figure 5**   Cross-sections through the two P-wave and two S-wave velocity models (GAP_P4, LLNL-G3Dv3, S362ANI, and TX2011) along

based S-wave velocity models to characterize subduction zone structures among other structural heterogeneities. Bearing such resolution differences in mind, the slab configurations are first figured out from the two P-wave velocity models, and then whether they are consistent with the images from the two S-wave velocity models examined. In Figure 5(a) and 5(b), the P-wave cross-sections across the Japan and Bonin arcs consistently show typical images of stagnant slabs above the 660-km discontinuity and the two S-wave cross-sections clearly support such an interpretation. The slab images in these subduction zones have been repeatedly revealed by P-wave tomography. See Fukao et al. (2001) for the earlier references including van der Hilst et al. (1991) and Fukao et al. (1992). More recent references include Miller et al. (2004), Huang and Zhao (2006), Li and van der Hilst (2010), van der Meer et al. (2010) and Zhao et al. (2009). Zhao et al. (2009) proposed the concept of the big mantle wedge by which they related the stagnant slabs to the widespread volcanism in eastern China. Li and van der Hilst (2010) related the horizontal spread of high-velocity anomalies in the transition zone to slab remnants since the Mesozoic Era.

Although the P-wave cross-sections across the Japan and Bonin arcs commonly show the images of stagnant slabs, the detailed slab configuration is very different. The downgoing slab beneath the Bonin arc dips more steeply and bends more sharply above the 660-km boundary than the slab beneath the Japan arc, as demonstrated in Figure 5(a) and 5(b), where the earthquake hypocenter distribution is superposed within a band 50 km wide on both sides of the cross-section plane, based on the EHB Bulletins published from the ISC (http://www.isc.ac.uk/ehbbulletin) (Engdahl et al., 1998). In the Bonin P-wave cross-sections (Figure 5(b)), the sharp bend of the slab image is correlated well with the bend of the deepest hypocentral distribution (Okino, et al., 1989). This correlation implies that the stagnant slab near the bending portion is brittle enough to cause earthquakes.

Figure 5(c) shows the cross-sections of the slab image of the Nazca plate along the east–west profile across Chile. Although the resolution is poorer here than in Japan and Bonin, the two P-wave velocity models consistently show the images of stagnant slab above the 660-km discontinuity. The earlier P-velocity models consistent with these images include those of Bijwaard et al. (1998) and Fukao et al. (2001). These stagnant slab images seem to be in better agreement with the fast anomaly pattern in the S-wave velocity model of S362ANI than of TX2011. Although the hypocentral distribution here shows a large gap between the intermediate-depth seismic zone and the deepest seismic zone, the P-wave velocity models seem to

profiles given in Figure 4. Structures are shown from Earth's surface down to the core–mantle boundary beneath (a) Japan, (b) Bonin, and (c) southern South America. For reference, thin lines at 410- and 660-km depths indicate the position of the discontinuities that define the mantle transition zone. An additional line at 1000 km does not mean a physically distinct boundary, but is drawn to give a rough measure of the bottom of the uppermost lower mantle. White dots depict hypocenters of earthquakes. Mantle earthquakes are considered to occur within subducted slabs. The scale of velocity anomaly is $\pm 1.5\%$ for the P-wave velocity models and $\pm 2.5\%$ for the S-wave velocity models.

suggest that the slab is continuous all the way through this seismicity gap. The deepest hypocenters extend subhorizontally in accordance with the stagnant slab images in the P-wave velocity models.

### 1.20.3.2  Slab Signature in the Uppermost Lower Mantle

Figure 6 shows the tomographic maps at depths of ~900 km in the uppermost lower mantle for the eight models corresponding to those in Figures 1 and 2 (see also Figure 3 of Panning and Romanowicz, 2006 for S-wave velocity anomalies and supplementary Figure 31(a) of Meer et al., 2009 for P- wave velocity anomalies). The Circum-Pacific subduction belt is still characterized by fast anomalies, both in the S-wave and the P-wave velocity models, although the intensities are, in general, weaker than those in the transition zone. The strongest anomalies in the western Pacific are now shifted southward to

the Indonesia–Philippine subduction zones, and those in South America are shifted northward to northern South America.

Figure 7(a)–7(c) shows the tomographic cross-sections across Java, Kermadec, and northern South America, respectively, for two P-wave velocity models, GAP_P4 and LLNL-G3Dv3, and for two S-wave velocity models, TX2011 and S362ANI. See Fukao et al. (2001) for the earlier references for the Java slab images including Widiyantoro and van der Hilst (1996). More recent references include Replumaz et al. (2004), Li et al. (2008), van der Meer et al. (2010), and Widiyantoro et al. (2011). The cross-sections across the two P-wave velocity models and the S-wave velocity model TX2011 in Figure 7(a) indicate that the slab beneath western Java penetrates the 660-km discontinuity and then deflects subhorizontally in the uppermost lower mantle. The two P-wave velocity models show the subhorizontally deflected slab that extends not only
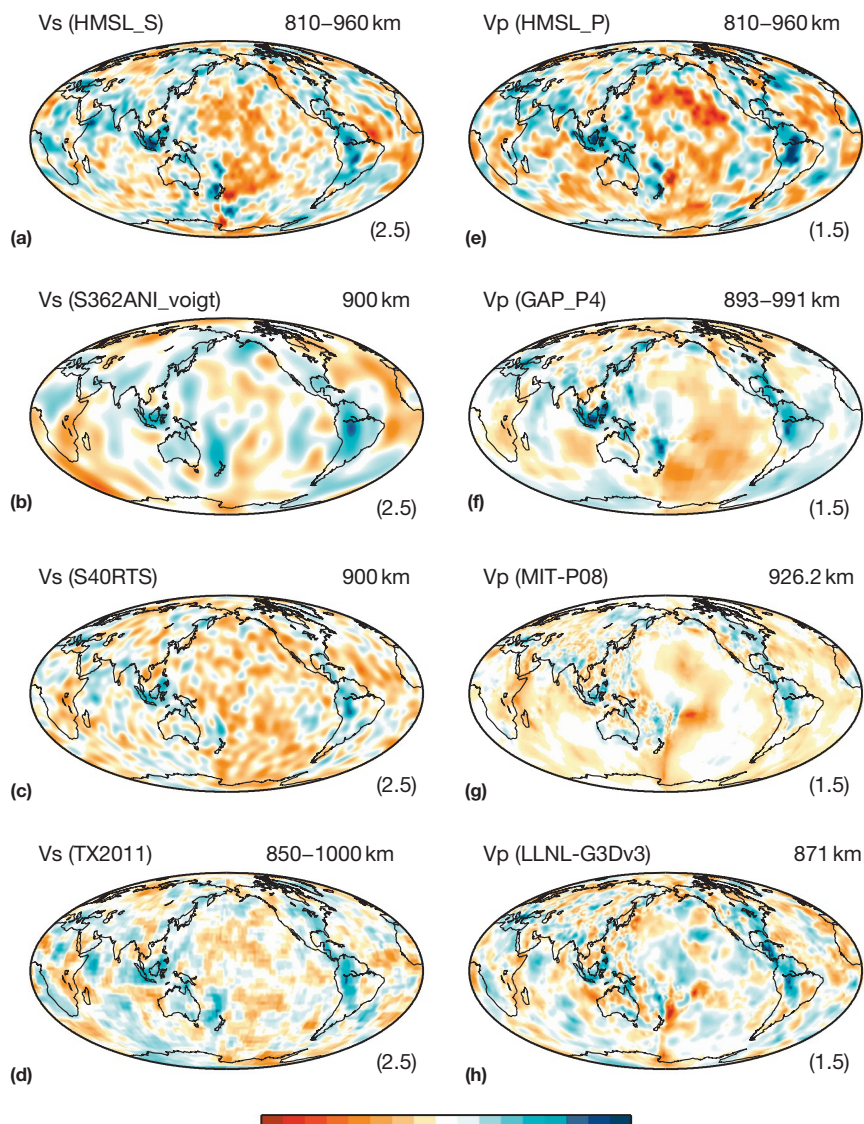


**Figure 6**  Depth slices in the uppermost lower mantle for the four S-wave and four P-wave velocity models corresponding to those in **Figure 1**. The velocities are perturbations from the average value at the corresponding depth. The scale is ±2.5% for the S-wave velocity models and ±1.5% for the P-wave velocity models.
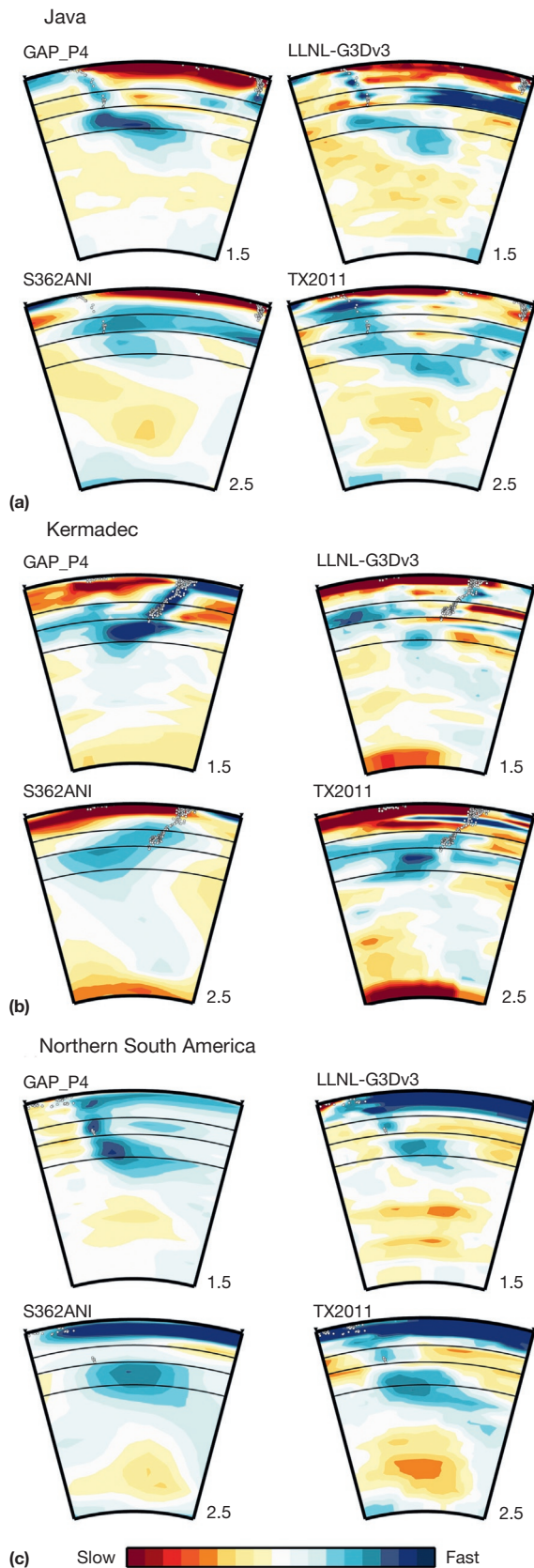
(a)



(b)



(c)

Slow ▰▰▰▰▰▰▰▰▰▰▰ Fast

**Figure 7** Cross-sections through the two P-wave and two S-wave velocity models (GAP_P4, LLNL-G3Dv3, S362ANI, and TX2011) along profiles given in **Figure 4**. Structures are shown from Earth's surface down to the core–mantle boundary beneath (a) Java, (b) Kermadec, and (c) northern South America. See **Figure 5** for other explanations.

in the forward direction but also slightly in the backward direction. Such a slab configuration may be related to the deep hypocentral distribution (at depths greater than ~500 km) that dips steeply in the slightly backward (southward) direction in agreement with the slightly backward orientation of the near-vertical compressional axes in the focal mechanisms of deep shocks (Das et al., 2000; Schöffel and Das, 1999). A slight backward spread of the slab image is also observed in **Figure 6** of Hafkenscheid et al. (2001) but not obvious in Replumaz et al. (2004) and Li et al. (2008). In **Figure 7(a)**, the two P-wave velocity models and the S-wave velocity model of TX2011 seem to indicate that the subhorizontally deflected slab begins to descend deeper, further beyond the uppermost lower mantle.

In **Figure 7(b)**, the P-wave velocity model of GAP-P4 shows an image of the subhorizontally deflected slab in the uppermost lower mantle beneath Kermadec. This slab image appears to be consistent with those of the two S-wave velocity models. These cross-sections seem to indicate that the subhorizontally deflected slab begins to descend to greater depths beyond the uppermost lower mantle. According to **Figure 4** of Schellart et al. (2009), which was constructed from the S-velocity model of Kennett and Gorbatov (2004) and the P-velocity model of Amaru (2007), this slab-related subhorizontal spread of high-velocity anomalies in the uppermost lower mantle extends further southward down to 27° S beneath the Tonga–Kermadec arc. The deepest hypocentral distribution in **Figure 7(b)** is more steeply dipping than at shallower depths. The downdip compression mechanisms of the deepest earthquakes (Alpert et al., 2010; Bonnardot et al., 2009; Brudzinski and Chen, 2005) suggest that the slab here is resisted by the surrounding mantle against its penetration across the 660-km discontinuity.

In **Figure 7(c)**, the two P-wave velocity models and the two S-wave velocity models consistently show the images of the Peruvian slab that penetrates the 660-km discontinuity, and then deflects subhorizontally in the uppermost lower mantle. The subhorizontally deflected slab seems to begin to descend deeper beyond the uppermost lower mantle. See Fukao et al. (2001) for the earlier references for the Peruvian slab images including Engdahl et al. (1995). Slab penetration is clearly imaged but subhorizontal deflection of the penetrated slab is less clear in a recent P-velocity model of Li et al. (2008). Seismic activity is very high within the penetrating slab in the proximity of the 660-km discontinuity. Although the deepest seismicity is well isolated from the shallower seismicity (see Brudzinski and Chen, 2005; Martinod et al., 2010), the tomographic cross-sections in the two P-wave velocity models seem to suggest that the slab continues through the seismicity gap between the shallow and deepest seismic zones. Earthquakes at greatest depths are of downdip compression type with steep compressional axes (average plunge = 79°; Brudzinski and Chen, 2005), suggesting that the slab here is resisted by the surrounding mantle against its steep penetration across the 660-km discontinuity.

### 1.20.3.3  Juxtaposed Slab Images in the Transition Zone and the Uppermost Lower Mantle

Figures 5 and 7 represent typical images of slabs deflected horizontally in the transition zone and those deflected subhorizontally in the uppermost lower mantle, respectively. The subduction zone in northern Tonga is unique in this respect, because the horizontal slab in the transition zone and the subhorizontal slab in the uppermost lower mantle may be juxtaposed in the same area. Figure 8 shows this possible juxtaposition. See Fukao et al. (2001) for the earlier references for the slab image beneath northern Tonga including van der Hilst (1995). More recent references include Hall and Spakman (2002) and Amaru (2007), which show similar slab features. Note that the deepest seismic zone here apparently splits into two, one extending at a very shallow dip and the other dipping very steeply. More detailed studies of the deep seismicity and focal mechanisms (e.g., Bonnardot et al., 2009; Brudzinski and Chen, 2005; Richards et al., 2011) suggest that the shallowly dipping seismic zone represents either the northern segment of the slab from the Tonga trench or the slab from the Vanuatu trench and that the steeply dipping seismic zone represents the southern segment of the slab from the Tonga trench. Fukao and Obayashi (2013) interpreted these two seismic zones as an indication of juxtaposition of two separate slabs, rather than a doubly thickened slab: one is stagnant above the 660-km discontinuity and the other is deflecting subhorizontally just below the discontinuity, as observed in northern Kermadec (Figure 7(b)). Deep shocks occurring within the stagnant slab in the transition zone are characterized by slab-parallel compression mechanisms such that the compressional axes are oriented on the average at an azimuth
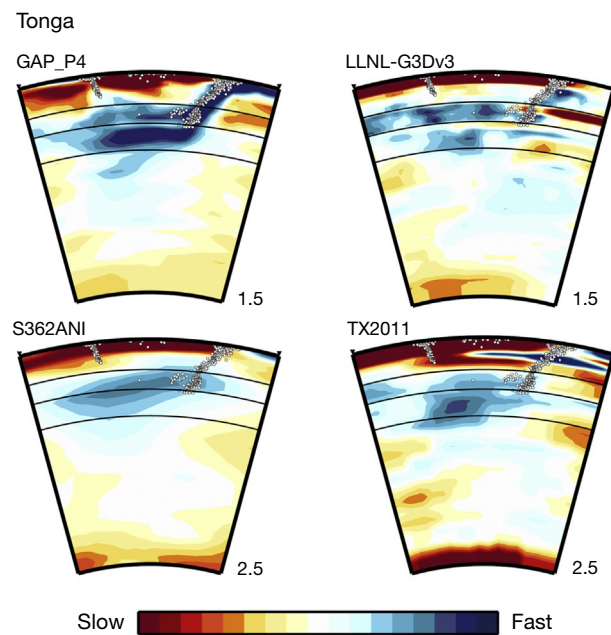


Tonga

**Figure 8**  Cross-sections through the two P-wave and two S-wave velocity models (GAP_P4, LLNL-G3Dv3, S362ANI, and TX2011) along a profile given in Figure 4. Structures are shown from Earth's surface down to the core–mantle boundary beneath northern Tonga. See Figure 5 for other explanations.

of 262° and an extremely shallow dip of 5° in the northern part and at an azimuth of 309° and a relatively shallow dip of 18° in the southern part (Bonnardot et al., 2009). These mechanisms imply that the stagnant slab here is resisted against its subhorizontal advance by the surrounding mantle.

### 1.20.4  Seismic Images of Slab Descent Through the Transition Zone

#### 1.20.4.1  Images of Transitional State from Slab Stagnation to Penetration

Seismic images of horizontally deflected slabs (stagnant slabs) in the transition zone (Figure 5) and subhorizontally deflected slabs in the uppermost lower mantle (Figure 7) have been overviewed so far. These images are understood to be the images of subducted slabs before and after the slab penetration. To answer the question of how a slab begins to penetrate the 660-km discontinuity and how it begins to deflect subhorizontally in the uppermost lower mantle, Figure 9(a) and 9(b) shows the cross-sections across the central Kurile arc and the central Mariana arc, respectively (see Fukao et al., 1992; van der Hilst et al., 1991 for the earliest images and van der Hilst and Seno, 1993 for the early attempts to explain the along-arc variation of slab morphology). The Kurile slab is well known to be horizontally deflected above the 660-km discontinuity in southern Kurile but penetrating the discontinuity in northern Kurile, as demonstrated by Figure 10 of Li et al. (2008), Figure 2 of Zhao et al. (2010), and Figure 5 of Fukao and Obayashi (2013). We may anticipate some transitional state from slab stagnation to penetration in central Kurile. In Figure 9(a), the two P-wave velocity models show the images of stagnant and penetrating slabs simultaneously, although LLNL-G3Dv3 emphasizes the stagnant slab, whereas GAP_P4 emphasizes the penetrating slab. The two S-wave velocity models seem to be more consistent with LLNL-G3Dv3 than with GAP_P4.

Also well known is the fact that the steeply dipping downgoing slab is bent to sharply horizontal at depths above the 660-km discontinuity beneath the Bonin arc, whereas it penetrates the discontinuity beneath the Mariana arc, as demonstrated by Figure 4 of Miller et al. (2004), Figure 10 of Li et al. (2008), and Figure 3 of Fukao and Obayashi (2013). Figure 9(b) shows the cross-sections across the central Mariana arc. The resolution of GAP_P4 has been improved in this region by the data from broadband ocean-bottom seismometers deployed in the Philippine Sea region (Obayashi et al., 2013). This model shows the image of the downgoing slab that penetrates the 660-km discontinuity and then enlarges horizontally in the uppermost lower mantle. It also shows the image of the stagnant slab above the discontinuity apparently detached from the downgoing slab. Such coexistence of the penetrated slab below and the stagnant slab above the discontinuity is faintly indicated in the images of V LLNL-G3Dv3 and TX2011. Model S362ANI seems to emphasize the stagnant slab more than the penetrating slab. Clearly, the lateral and vertical resolutions of the existing models are still too limited to detect the fine structure at the possible transitional stage from slab stagnation to penetration in the central Kurile and central Mariana regions.
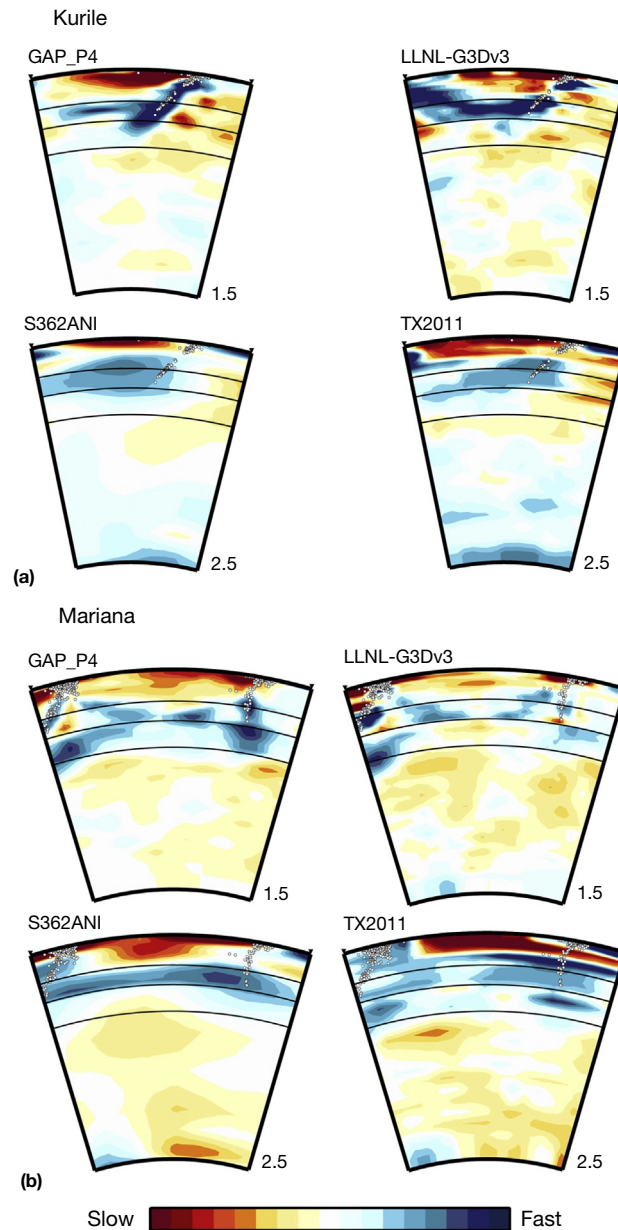
**Figure 9**   Cross-sections through the two P-wave and two S-wave velocity models (GAP_P4, LLNL-G3Dv3, S362ANI, and TX2011) along profiles given in **Figure 4**. Structures are shown from Earth's surface down to the core–mantle boundary beneath (a) central Kurile and (b) central Mariana. See **Figure 5** for other explanations.

### 1.20.4.2    Signature of Subducted Crust Materials in the Penetrating Slab

Some observational evidence indicates that a penetrating slab has fragments of subducted crust materials within it. Niu et al. (2003) detected an ~10-km thick S-to-P reflector at a depth of ~1150 km beneath the northern Mariana arc, using a Japanese short-period seismic network. They interpreted this reflector as a fragment of the oceanic crust internally displaced to the bottom of the penetrating slab. Kaneshima (2003) detected S-to-P scatterers at depths of 700–900 km beneath the central Mariana arc, using two short-period seismic arrays in the United States. All the scatterers, including those detected by

Krüger et al. (2001), were located inside the deformed body of the penetrating slab. Kaneshima (2009) detected S-to-P scatterers in a depth range of 800–1000 km beneath the northern Kurile arc. He located the scatterers near the bottom of the enlarged body of the penetrating slab and interpreted them as the remnants of subducted oceanic crust. Rost et al. (2008) used off-great-circle-path precursors to PP-waves (P-waves reflected off the surface once) recorded by a Canadian short-period seismic array to detect P-to-P scatterers. They showed that these scatterers are located mostly at depths shallower than 1000 km and in large part in the Mariana subduction zone. Rost et al. (2008) interpreted these scatterers as being from the
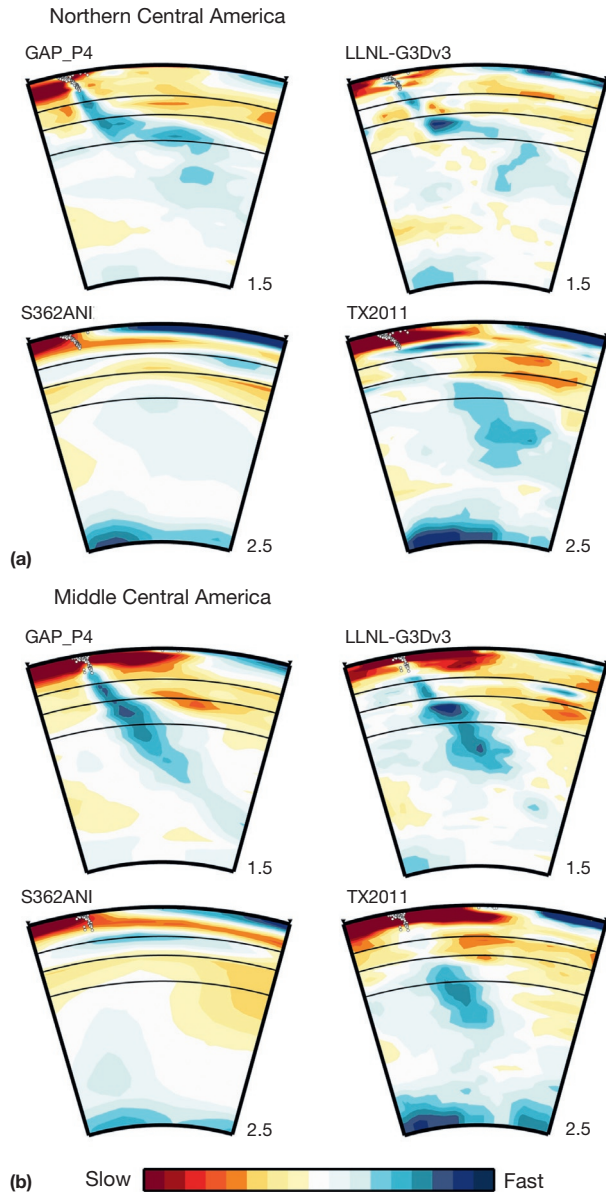
Northern Central America

GAP_P4

LLNL-G3Dv3

1.5

1.5

S362ANI

TX2011

**(a)**

2.5

2.5

Middle Central America

GAP_P4

LLNL-G3Dv3

1.5

1.5

S362ANI

TX2011

2.5

2.5

**(b)**    Slow ▮▮▮▮▮▮▮▮▮▮▮▮▮ Fast

**Figure 10**   Cross-sections through the two P-wave and two S-wave velocity models (GAP_P4, LLNL-G3Dv3, S362ANI, and TX2011) along profiles given in **Figure 4**. Structures are shown from Earth's surface down to the core–mantle boundary beneath (a) northern Central America and (b) middle Central America. See **Figure 5** for other explanations.

### 1.20.4.3    Images of Slab Descent to the Deep Lower Mantle

The Central American subduction zone is the best place to observe images of slab descent all the way through the transition zone, the uppermost lower mantle, and the deep lower mantle. Tomographic images of the deeply subducted slab under this region have been repeatedly reported (Grand, 2002; Li et al., 2008; Ren et al., 2007; see Fukao et al. (2001) for the earlier references including van der Hilst et al., 1997 and Grand et al., 1997). **Figure 10(a)** and **10(b)** shows the cross-sections across the northern and middle Central American arcs, respectively. In **Figure 10(a)**, GAP_P4 and LLNL-G3Dv3 show slab configurations remarkably similar to each other. The downgoing slab penetrates the 660-km discontinuity, thereby deflecting to horizontal below the discontinuity, and is then apparently folded down into the deeper mantle. This deeper part of the slab is emphasized more in TX2011 than in the two P-wave velocity models. In **Figure 10(b)**, the slab configurations shown by GAP_P4, LLNL-G3Dv3, and TX2011 are remarkably similar to each other (see also Li et al., 2008). The slab extends almost straight through the intermediate-depth seismic zone downdip to mid-mantle depths of approximately 1500 km. Fukao and Obayashi (2013) interpreted the slab configurations in **Figure 10(a)** and **10(b)** as those at the relatively earlier and later stages of deep slab subduction.

### 1.20.5    Summary

The mantle transition zone acts as a (temporal) reservoir for subducting slabs of lithospheric plates, as typically observed in Japan, Bonin, and southern South America (**Figure 5**). Increasing evidence suggests that the uppermost lower mantle acts as another (temporal) reservoir for subducting slabs, although its bottom is defined only loosely. The typical subduction zone of this type includes Java, Kermadec, and northern South America, where the penetrated slab is deflected subhorizontally in the uppermost lower mantle (**Figure 7**). One can observe the juxtaposition of a horizontal slab above the 660-km discontinuity and a subhorizontal slab below the discontinuity beneath the northern Tonga arc (**Figure 8**). In general, slabs in central Kurile and central Mariana are not well resolved, but the images give some idea of how the transition from slab stagnation to penetration occurs (**Figure 9**). Some evidence indicates that slabs trapped in the deeper reservoir are severely deformed internally so that the subducted oceanic crust is fragmented into scattered pieces.

A remarkable correlation exists between the slab image in the transition zone and the deepest hypocentral distribution (Fukao and Obayashi, 2013). The dip of the deepest hypocentral distribution often deviates from the dip of the major seismic zone. In the case of a horizontally deflected slab above the 660-km discontinuity, the deepest hypocentral distribution tends to dip more gently than the shallower portion of the seismic zone (see the cross-sections across Bonin and Chile in **Figure 5**). In the case of a subhorizontally deflected slab below the discontinuity, the deepest hypocentral distribution tends to dip more steeply than the shallower part of the seismic zone (see the cross-sections across Java, Kermadec, and Peru in **Figure 7**). This is also the case of a downgoing slab

paleo-Moho (the Moho is the boundary between the crust and the mantle) of the deeply subducted slabs. Although they did not show where these scatterers are located relative to the penetrated slab, all the other studies cited earlier located fragments of the subducted crust within or at the bottom of the penetrating slab rather than at the top. This location suggests that slab penetration and subsequent processes are associated with severe deformation within the slab. The penetrated crust may no longer be a coherent unit at the top of the slab.

beginning to penetrate the discontinuity or beginning to spread laterally below it (see the cross-sections across central Kurile and central Mariana in Figure 9). In the case where the slab images suggest juxtaposition of the horizontal slab above the 660 and the subhorizontal slab below the 660, the deepest hypocentral distribution apparently splits into two, one dipping very gently and the other dipping very steeply (see the cross-section across Tonga in Figure 8).

Downgoing slabs tend to be deflected horizontally in the transition zone, and penetrated slabs tend to be deflected subhorizontally. The transition zone and the uppermost lower mantle are thus two distinct reservoirs of subducted slabs. Together they constitute a chain of slab reservoirs around the Circum-Pacific; however, both allow slab leakage from the bottom. The deeply descending slab images beneath Central America (Figure 10) may be understood as an extreme case of slab leakage from the bottom of the uppermost lower mantle well into the mid-lower mantle. While either the transition zone or the uppermost lower mantle serves as a slab reservoir, only the former acts as a reservoir of water. The water solubility in the major mineral of the transition zone is ~3.3 wt% (wadsleyite) to ~2.6 wt% (ringwoodite), whereas it is only <30 ppm (Mg-perovskite) to <100 ppm (ferropericlase) in the major mineral of the uppermost lower mantle (Litasov et al., 2006). Even if the slab in the transition zone contains a significant amount of water, water should be expelled from the slab upon penetration across the 660-km discontinuity. At present, however, there is no consensus on how and to what extent water is carried down into the transition zone with the subducting slab (Jacobsen and van der Lee, 2006; Kawakatsu and Yoshioka, 2011; Meier et al., 2009; Tonegawa et al., 2008).

## Acknowledgments

## References

Alpert LA, Becker TW, and Bailey LW (2010) Global slab deformation and centroid moment tensor constraints on viscosity. *Geochemistry, Geophysics, Geosystems* 11. http://dx.doi.org/10.1029/2010GC003301.

Amaru M (2007) *Global Travel Time Tomography with 3-D Reference Models*. PhD Thesis. Utrecht: Utrecht University. http://igitur-archive.library.uu.nl/dissertations/2007-0202-201924/c5.pdf.

Bijwaard H, Spakman W, and Engdahl ER (1998) Closing the gap between regional and global tomography. *Journal of Geophysical Research* 103: 30005–30078.

Bonnardot MA, Régnier M, Christova C, Ruellan E, and Tric E (2009) Seismological evidence for a slab detachment in the Tonga subduction zone. *Tectonophysics* 464: 84–99.

Brudzinski MR and Chen WP (2005) Earthquakes and strain in subhorizontal slabs. *Journal of Geophysical Research* 110. http://dx.doi.org/10.1029/2004JB003470.

Dahlen FA, Hung SH, and Nolet G (2000) Frechet kernels for finite-frequency traveltimes – I. Theory. *Geophysical Journal International* 141: 157–174.

Dalton CL, Ekström G, and Dziewonski AM (2008) The global attenuation structure of the upper mantle. *Journal of Geophysical Research* 113. http://dx.doi.org/10.1029/2007JB005429.

Das S, Schöffel HJ, and Gilbert F (2000) Mechanism of slab thickening near 670 km under Indonesia. *Geophysical Research Letters* 27: 831–834.

Dunn RA and Forsyth DW (2007) Crust and lithospheric structure – Seismic structure of mid-oceanic ridges. In: Romanowicz B and Dziewonski AM (eds.) *Seismology and the Structure of the Earth. Treatise on Geophysics*, vol. 1, pp. 419–443. Amsterdam: Elsevier.

Dziewonski AM and Romanowicz B (2007) Overview. In: Romanowicz B and Dziewonski AM (eds.) *Seismology and the Structure of the Earth. Treatise on Geophysics*, vol. 1, pp. 1–29. Amsterdam: Elsevier.

Engdahl ER, van der Hilst R, and Berrocal J (1995) Imaging of subducted lithosphere beneath South America. *Geophysical Research Letters* 22: 2317–2320.

Engdahl ER, van der Hilst R, and Buland R (1998) Global teleseismic earthquake relocation with improved travel times and procedures for depth determination. *Bulletin of the Seismological Society of America* 88: 722–743.

Faccenna C, Becker TW, Lucente FP, Jolivet L, and Rossetti F (2001) History of subduction and back-arc extension in the Central Mediterranean. *Geophysical Journal International* 145: 809–820.

Ferreira AMG, Woodhouse JH, Visser K, and Trampert J (2010) On the robustness of global radially anisotropic surface wave tomography. *Journal of Geophysical Research* 115. http://dx.doi.org/10.1029/2009JB006716.

Fukao Y and Obayashi M (2013) Subducted slabs stagnant above, penetrating through and trapped below the 660-km discontinuity. *Journal of Geophysical Research*, under review.

Fukao Y, Obayashi M, Inoue H, and Nenbai M (1992) Subducting slabs stagnant in the mantle transition zone. *Journal of Geophysical Research* 97: 4809–4822.

Fukao Y, Obayashi M, Nakakuki T, and Deep Slab Project Group. (2009) Stagnant slab: A review. *Annual Reviews of Earth and Planetary Sciences* 37: 19–46.

Fukao Y, Widiyantoro S, and Obayashi M (2001) Stagnant slabs in the upper and lower mantle transition region. *Review of Geophysics* 39: 291–323.

Funiciello F, Faccenna C, Heuret A, Lallemand S, Giuseppe ED, and Becker TW (2008) Trench migration, net rotation and slab–mantle coupling. *Earth and Planetary Science Letters* 271: 233–240.

Grand SP (2002) Shear-wave tomography and the fate of subducted slabs. *Philosophical Transactions of the Royal Society of London A* 360: 2475–2481.

Grand SP, van der Hilst RD, and Widiyantoro S (1997) Global seismic tomography: A snapshot of convection in the Earth. *Geological Society of America Today* 7: 1–7.

Gu YJ, Okeler A, and Schultz R (2012) Tracking slabs beneath northwestern Pacific subduction zones. *Earth and Planetary Science Letters* 331–332: 269–280.

Gung Y and Romanowicz B (2004) Q tomography of the upper mantle using three-component long-period waveforms. *Geophysical Journal International* 157: 813–830.

Hafkenscheid E, Buiter SJH, Wortel MJR, Spakman W, and Bijwaard H (2001) Modeling the seismic velocity structure beneath Indonesia: A comparison with tomography. *Tectonophysics* 333: 35–46.

Hall R and Spakman W (2002) Subducted slabs beneath the eastern Indonesia-Tonga region: Insights from tomography. *Physics of the Earth and Planetary Interiors* 201: 321–336.

Heit B, Yuan X, Bianchi M, Kind R, and Gossler J (2010) Study of the lithospheric and upper-mantle discontinuities beneath eastern Asia by *SS* precursors. *Geophysical Journal International* 183: 252–266.

Houser C, Masters G, Flanagan M, and Shearer P (2008) Determination and analysis of long-wavelength transition zone structure using *SS* precursors. *Geophysical Journal International* 174: 178–194.

Houser C, Masters G, Shearer P, and Laske G (2008) Shear and compressional velocity models of the mantle from cluster analysis of long-period waveforms. *Geophysical Journal International* 174: 195–212.

Huang J and Zhao D (2006) High-resolution mantle tomography of China and surrounding regions. *Journal of Geophysical Research* 111. http://dx.doi.org/10.1029/2005JB004066.

Iidaka T and Suetsugu D (1992) Seismological evidence for metastable olivine inside a subducting slab. *Nature* 356: 593–595.

Jacobsen SD and van der Lee S (2006) Earth's deep water cycle. *Geophysical Monograph*, vol. 168, 313 pp. Washington, DC: American Geophysical Union.

Jiang G, Zhao D, and Zhang G (2008) Seismic evidence for a metastable olivine wedge in the subducting Pacific slab under Japan Sea. *Earth and Planetary Science Letters* 270: 300–307.

Kaneshima S (2003) Small-scale heterogeneity at the top of the lower mantle around the Mariana slab. *Earth and Planetary Science Letters* 209: 85–101.

Kaneshima S (2009) Seismic scatterers at the shallowest lower mantle beneath subducted slabs. *Earth and Planetary Science Letters* 286: 304–315.

Kaneshima S, Okamoto T, and Takenaka H (2007) Evidence for a metastable olivine wedge inside the subducted Mariana slab. *Earth and Planetary Science Letters* 258: 219–227.

Kárason H and van der Hilst RD (2001) Tomographic imaging of the lowermost mantle with differential times of refracted and diffracted core phases (PKP, Pdiff ). *Journal of Geophysical Research* 106: 6569–6588. http://dx.doi.org/10.1029/2000JB900380.

Kawakatsu H and Yoshioka S (2011) Metastable olivine wedge and deep dry cold slab beneath southwest Japan. *Earth and Planetary Science Letters* 303: 1–10.

Kawazoe T, Ohuchi T, Nishihara Y, Nishiyama N, Fujino K, and Irifune T (2013) Seismic anisotropy in the mantle transition zone induced by shear deformation of wadsleyite. *Physics of the Earth and Planetary Interiors* 216: 91–98.

Kennett BLN and Gorbatov A (2004) Seismic heterogeneity in the mantle – Strong shear wave signature of slabs from joint tomography. *Physics of the Earth and Planetary Interiors* 146: 87–100.

Kind R and Li X (2007) Deep Earth structure – Transition zone and mantle discontinuities. In: Romanowicz B and Dziewonski AM (eds.) *Seismology and the Structure of the Earth*. *Treatise on Geophysics*, vol. 1, pp. 591–618. Amsterdam: Elsevier.

Kirby SH, Stein S, Okal EA, and Rubie D (1996) Metastable mantle phase transformations and deep earthquakes in subducting oceanic lithosphere. *Reviews of Geophysics* 34: 261–306.

Koper KD, Wiens DA, Dorman LM, Hildebrand JA, and Webb SC (1998) Modeling the Tonga slab: Can travel time data resolve a metastable olivine wedge? *Journal of Geophysical Research* 103: 30079–30100.

Krüger FK, Baumann M, Scherbaum F, and Weber M (2001) Mid mantle scatterers near the Mariana slab detected with a double array method. *Geophysical Research Letters* 28: 667–670.

Kustowski B, Ekström G, and Dziewonski AM (2008) Anisotropic shear-wave velocity structure of the Earth's mantle: A global model. *Journal of Geophysical Research* 113. http://dx.doi.org/10.1029/2007JB005169.

Lekić V and Romanowicz B (2011) Inferring upper-mantle structure by full waveform tomography with the spectral element method. *Geophysical Journal International* 185: 799–831.

Li C and van der Hilst RD (2010) Structure of the upper mantle and transition zone beneath Southeast Asia from traveltime tomography. *Journal of Geophysical Research* 115. http://dx.doi.org/10.1029/2009JB006882.

Li C, van der Hilst RD, Engdahl ER, and Burdick S (2008) A new global model for P wave speed variations in Earth's mantle. *Geochemistry, Geophysics, Geosystems* 9. http://dx.doi.org/10.1029/2007GC001806.

Litasov KD, Ohtani E, and Sano A (2006) Influence of water on major phase transitions in the Earth's mantle. In: Jacobsen SD and van der Lee S (eds.) *Earth's Deep Water Cycle*. *Geophysical Monograph*, vol. 168, pp. 95–111. Washington, DC: American Geophysical Union.

Lithgow-Bertelloni C and Richard MC (1998) The dynamics of Cenozoic and Mesozoic plate motions. *Review of Geophysics* 36: 27–78.

Martinod J, Husson L, Roperch P, Guillaume B, and Espurt N (2010) Horizontal subduction zones, convergence velocity and the building of the Andes. *Earth and Planetary Science Letters* 299: 299–309.

Masters G, Jordan TH, Silver PG, and Gilbert F (1982) Aspherical Earth structure from fundamental spheroidal-mode data. *Nature* 298: 609–613.

Meier U, Trampert J, and Curtis A (2009) Global variations of temperature and water content in the mantle transition zone from higher mode surface waves. *Earth and Planetary Science Letters* 282: 91–101.

Mercerat ED and Nolet G (2013) On the linearity of cross-correlation delay times in finite-frequency tomography. *Geophysical Journal International* 192: 681–687.

Miller MS, Kennett BLN, and Lister GS (2004) Imaging changes in morphology, geometry, and physical properties of the subducting Pacific plate along the Izu–Bonin–Mariana arc. *Earth and Planetary Science Letters* 224: 363–370.

Montagner JP (2007) Upper mantle structure: Global isotropic and anisotropic tomography. In: Romanowicz B and Dziewonski AM (eds.) *Seismology and Structure of the Earth*. *Treatise on Geophysics*, vol. 1, pp. 559–589. Amsterdam: Elsevier.

Niu F, Kwakatsu H, and Fukao Y (2003) Seismic evidence for a chemical heterogeneity in the midmantle: A slightly dipping and strong seismic reflector at mid-depth beneath the Mariana subduction zone. *Journal of Geophysical Research* 108. http://dx.doi.org/10.1029/2002JB002384.

Obayashi M, Yoshimitsu J, Nolet G, et al. (2013) Finite frequency whole mantle P-wave tomography: Improvement of subducted slab images. *Geophysical Research Letters* 40: 5652–5657. http://dx.doi.org/10.1002/2013GL057401.

Okino K, Ando M, Kaneshima S, and Hirahara K (1989) The horizontally lying slab. *Geophysical Research Letters* 16: 1059–1062.

Panning M and Romanowicz B (2006) A three-dimensional radially anisotropic model of shear velocity in the whole mantle. *Geophysical Journal International* 167: 361–379.

Ren Y, Stutzmann E, van der Hilst RD, and Besse J (2007) Understanding seismic heterogeneities in the lower mantle beneath the Americas from seismic tomography and plate tectonic history. *Journal of Geophysical Research* 112. http://dx.doi.org/10.1029/2005JB004154.

Replumaz A, Kárson H, van der Hilst RD, Besse J, and Tapponnier P (2004) 4-D evolution of SE Asia's mantle from geological reconstructions and seismic tomography. *Earth and Planetary Science Letters* 221: 103–115.

Richards MA and Engebretson DC (1992) Large-scale mantle convection and the history of subduction. *Nature* 355: 437–440.

Richards S, Holm R, and Barber G (2011) When slabs collide: A tectonic assessment of deep earthquakes in the Tonga–Vanuatu region. *Geology* 39: 787–790.

Ritsema J, Deuss A, van Heijst HJ, and Woodhouse JH (2011) S40RTS: A degree-40 shear-velocity model for the mantle from new Rayleigh wave dispersion, teleseismic travel time and normal-mode splitting function measurements. *Geophysical Journal International* 184: 1223–1236.

Romanowicz B (1990) The upper mantle degree 2: Constraints and inferences from global mantle wave attenuation measurements. *Journal of Geophysical Research* 95: 11051–11071.

Romanowicz B and Mitchell BJ (2007) Deep Earth structure – Q of the Earth from crust to core. In: Romanowicz B and Dziewonski AM (eds.) *Seismology and the Structure of the Earth*. *Treatise on Geophysics*, vol. 1, pp. 731–774. Amsterdam: Elsevier.

Rost S, Garnero EJ, and Williams Q (2008) Seismic array detection of subducted oceanic crust in the lower mantle. *Journal of Geophysical Research* 113. http://dx.doi.org/10.1029/2007JB005263.

Schmerr N and Garnero EJ (2007) Upper mantle discontinuity topography from thermal and chemical heterogeneity. *Science* 318: 623–626.

Schmerr N and Thomas C (2011) Subducted lithosphere beneath the Kuriles from migration of PP precursors. *Earth and Planetary Science Letters* 311: 101–111.

Schöffel HJ and Das S (1999) Fine details of the Wadati–Benioff zone under Indonesia and its geodynamic implications. *Journal of Geophysical Research* 104: 13101–13114.

Selby ND and Woodhouse JH (2002) The Q structure of the upper mantle: Constraints from Rayleigh wave amplitudes. *Journal of Geophysical Research* 107. http://dx.doi.org/10.1029/2001JB000257.

Shearer P (1993) Global mapping of upper mantle reflectors from long period *SS* precursors. *Geophysical Journal International* 115: 878–904.

Shearer P and Masters G (1992) Global mapping of topography on the 660-km discontinuity. *Nature* 355: 791–796.

Simmons NA, Myers SC, Johannesson G, and Matzel E (2012) LLNL-G3Dv3: Global P wave tomography model for improved regional and teleseismic travel time prediction. *Journal of Geophysical Research* 117. http://dx.doi.org/10.1029/2012JB009525.

Stixrude L and Jeanloz R (2007) Constraints on seismic models from other disciplines – Constraints from mineral physics on seismological models. In: Romanowicz B and Dziewonski AM (eds.) *Seismology and the Structure of the Earth*. *Treatise on Geophysics*, vol. 1, pp. 775–803. Amsterdam: Elsevier.

Sung CM and Burns RG (1976) Kinetics of high pressure phase transformations: Implications to the evolution of olivine–spinel transition in the downgoing lithosphere and its consequences on the dynamics of the mantle. *Tectonophysics* 31: 1–32.

Thurber C and Ritsema J (2007) Theory and observations – Seismic tomography and inverse methods. In: Romanowicz B and Dziewonski AM (eds.) *Seismology and the Structure of the Earth*. *Treatise on Geophysics*, vol. 1, pp. 323–360. Amsterdam: Elsevier.

Tonegawa T, Hirahara K, Shibutani T, Iwamori H, Kanamori H, and Shiomi K (2008) Water flow to the mantle transition zone inferred from a receiver function image of the Pacific slab. *Earth and Planetary Science Letters* 274: 346–354.

van der Hilst R (1995) Complex morphology of subducted lithosphere in the mantle beneath the Tonga trench. *Nature* 374: 154–157.

van der Hilst R, Engdahl R, Spakman W, and Nolet G (1991) Tomographic imaging of subducted lithosphere below northwest Pacific island arcs. *Nature* 353: 37–43.

van der Hilst R and Seno T (1993) Effects of relative plate motion on the deep structure and penetration depth of slabs below the Izu–Bonin and Mariana island arcs. *Earth and Planetary Science Letters* 120: 375–407.

van der Hilst R, Widiyantoro S, and Engdahl R (1997) Evidence for deep mantle circulation from global tomography. *Nature* 386: 578–584.

van der Meer DG, Spakman W, van Hinsbergen DJJ, Amaru ML, and Torsvik TH (2010) Towards absolute plate motions constrained by lower-mantle slab remnants. *Nature Geoscience* 3: 36–40.

Visser K, Trampert J, Lebedev S, and Kennett BLN (2008) Probability of radial anisotropy in the deep mantle. *Earth and Planetary Science Letters* 270: 241–250.

Wen L and Anderson DL (1995) The fate of slabs inferred from seismic tomography and 130 million years of suduction. *Earth and Planetary Science Letters* 133: 185–198.

Wen L and Anderson DL (1997) Layered mantle convection: A model for geoid and topography. *Earth and Planetary Science Letters* 146: 367–377.

Widiyantoro S, Pesicek JD, and Thurber CH (2011) Subducting slab structure below the eastern Sunda arc inferred from non-linear seismic tomographic imaging. *Geological Society, London, Special Publications* 355: 139–155.

Widiyantoro S and van der Hilst R (1996) Structure and evolution of subducted lithosphere beneath the Sunda arc, Indonesia. *Science* 271: 1566–1570.

Zhao D, Pirajno F, Dobretsov NL, and Liu L (2010) Mantle structure and dynamics under East Russia and adjacent regions. *Russian Geology and Geophysics* 51: 925–938.

Zhao D, Tian Y, Lei J, Liu L, and Zheng S (2009) Seismic image and origin of the Changbai intraplate volcano in East Asia: Role of big mantle wedge above the stagnant Pacific slab. *Physics of the Earth and Planetary Interiors* 173: 197–206.